

Quaternary rainfall variability is governed by insolation in northern China and ice-sheet forcing in the South

Debo Zhao ^{1✉}, Zhengyao Lu ^{2✉}, Shiming Wan ^{1,3,4}, Hai Cheng ⁵, Xuefa Shi ⁶ & Anchun Li¹

Quaternary Asian low-latitude hydroclimate cyclicity has long been attributed to insolation forcing, in contrast to the dominant ice-sheet and CO₂ controls identified in mid-high-latitude regions. However, debates exist regarding these rainfall variations and forcings due to inconsistent reconstructions and simulations. Here, by combining rainfall proxy records with multi-model simulations, dominant 23 ka rainfall cycle in northern China and 100 ka rainfall cycle in southern China and Southeast Asia were found. We propose that rainfall mainly occurs in summer in the north, primarily driven by insolation. Rainfall in the south is largely forced by high-latitude ice sheets, with enhanced spring and autumn rainfall in southern China and weakened rainfall in western Maritime Continent during glacial periods. This study highlights the seasonal contributions to orbital-scale rainfall changes, and sheds light on the Asian hydroclimate conditions associated with high-low-latitude climate interactions.

¹Key Laboratory of Marine Geology and Environment, Institute of Oceanology, Chinese Academy of Sciences, Qingdao 266071, China. ²Department of Physical Geography and Ecosystem Science, Lund University, Sölvegatan 12, 22362 Lund, Sweden. ³Laboratory for Marine Geology, Qingdao National Laboratory for Marine Science and Technology, Qingdao 266061, China. ⁴CAS Center for Excellence in Quaternary Science and Global Change, Xi'an 710061, China. ⁵Institute of Global Environmental Change, Xi'an Jiaotong University, Xi'an 710054, China. ⁶Key Laboratory of Marine Sedimentology and Environmental Geology, First Institute of Oceanography, Ministry of Natural Resources, Qingdao 266061, China. ✉email: zhaodebo@qdio.ac.cn; zhengyao.lu@nateko.lu.se

Monsoons are seasonal variations in atmospheric circulations accompanied by the reversal of dry and wet surface climate conditions, and are mainly forced by seasonal pressure system shifts driven by the annual/seasonal solar radiative forcing cycle¹. Theoretically, precession forcing contributes more to the solar radiation amplitude received by Earth than obliquity or eccentricity², thus, the 23 ka cycle should be considered as the dominant mode affecting monsoon climate variations. This hypothesis has been tested in some early rainfall reconstruction and modeling studies in mid-low-latitude regions^{3–7}. In contrast, high-latitude hydroclimate conditions tend to respond to ice-sheet and CO₂ forcings as a result of multiple atmospheric processes, thus suggesting strong glacial-interglacial cycles of 100 ka in these regions^{8–10}.

Such latitude dependent forcing of monsoon hydroclimates has also been proposed in the East Asian monsoon region. Monsoon rainfall variabilities in the Loess Plateau and Yangtze River Valley in northern-central China are more sensitive to ice-sheet and CO₂ forcings and less sensitive to insolation forcing than that in southern China^{9,11–13}. This results in dominant 100 ka cycle of summer monsoon climate in northern China but 23 ka cycle in southern China. However, all recent precipitation isotope record reanalysis and model simulations have revealed that glacial-interglacial cycles are dominant in southern China^{14,15}, even in tropical Southeast Asia^{15–17}, highlighting the dominant ice sheet and CO₂ forcing on the lower latitude hydroclimate. Another paradox is that most previous simulation studies have suggested the existence of strong precession forcing on the East Asian monsoon hydroclimate^{18–23}. Even when ice-sheet and greenhouse gas forcings were included in these simulations, the dominant precession signal can still be observed in northern China^{14,24}. This can be supported by recently rainfall reconstructions in the Tengger Desert in northern China, which revealed prominent precession cycles in local rainfall variation, challenging the view that high-latitude ice sheets are the primary driver of northern China monsoon hydroclimate²⁵. Such controversial complicates our understanding of hydroclimate in East Asian monsoon domain and surrounding tropical climate zone associated with high-low-latitude climate interactions.

To address these conundrums, we present a silicate weathering record from Site U1429 (31°37.04'N, 128°59.85'E) of the International Ocean Discovery Program (IODP) in the northern East China Sea (Fig. 1a and Supplementary Fig. 1a) to quantitatively reconstruct the rainfall changes in northern China over the last 400 ka. We also analyzed a transient climate model simulation (comprising orbital (ORB) + greenhouse (GHG) + ice sheet (ICE) forcings) through the last 300 ka using the fully coupled National Center for Atmospheric Research-Community Climate System Model version 3 (NCAR-CCSM3) model^{26,27}, and studied the periodicity of simulated rainfall variations and the drivers of this periodicity in East-Southeast Asia. In addition, we compared the Transient Climate Evolution (TraCE)-21ka simulation (and the individual forcing simulations) performed using the same model^{28,29} and iTraCE based on an isotope-enabled Community Earth System Model (iCESM)^{30–32} to assess the hydroclimatic changes across East-Southeast Asia, focusing on the individual forcing mechanisms and isotope-climate relationship, respectively.

Results and discussion

Dominant precession cyclicity of rainfall variability in northern China. It is feasible to reconstruct the rainfall series in northern China based on silicate weathering record derived from IODP Site U1429, due to the robust sediment provenance tracing results based on Nd isotopic and rare earth element compositions;

these results suggest that the Yellow River in northern China is the major supplier of clay-sized sediments in the study region (Supplementary Figs. 1a and 2) (Supplementary Discussion). The Yellow River has long been regarded as a typical river influenced by intense catchment erosion. It is globally known for its high sediment flux (~11 billion ton/yr, before 1980s) sourced dominantly from the Chinese Loess Plateau (~90% of sediments) in the middle reach of this river^{33,34}. Such huge loess materials supply makes the effect from eolian dust on Yellow River sediment composition can be ignored. Thus chemical alteration of sediments during transport from Loess Plateau to our study site has the potential to record local hydroclimate changes.

The chemical weathering intensity can be calculated by comparing the concentration of mobilized elements (K) to a non-mobile element (Al) during incongruent weathering of silicates³⁵. Lower K-to-Al ratios (K/Al) indicate greater mobile element depletion in sediments and thus higher chemical alteration. The Yellow River basin has an arid to semi-arid continental climate, being more arid and cold in the upper and middle reaches, and more humid and temperate in the lower reaches. Here we selected surface sediment samples distribute from upper to lower reaches of Yellow River (Supplementary Fig. 1a). High linear correlations have been observed between the K/Al ratios of clay-sized sediments and mean annual temperature and rainfall at each site, suggesting the controlling effects of temperature and rainfall on the silicate weathering intensity (Supplementary Fig. 1b, c). Sediment samples of Yellow River and Site U1429 were all analyzed on the clay-sized fraction, which avoids the grain-size effect on their chemical composition. Effect of physical erosion on chemical weathering has also been excluded (Supplementary Discussion). Here, we established a model covering K/Al ratio, temperature and rainfall based on the multiple statistical analyses, and further quantitatively calculated the rainfall changes during the last 400 ka (Supplementary Discussion). The calculated mean annual rainfall ranges from ~470–717 mm (Fig. 2c). This is close to the modern annual rainfall (~562–648 mm) in the Yellow River middle to lower reaches³⁶ and our simulated annual rainfall amount (~407–854 mm) in northern China (Fig. 2c, d).

Our rainfall reconstruction result suggests a distinct story compared to the findings of most previous studies. It shows strong precession cycle and is consistent with the 300 ka simulation results of annual rainfall in northern China (Fig. 2c, d). This differs from the loess magnetic susceptibility, a classic summer monsoon rainfall proxy, and from existing records of loess carbon and beryllium isotopes (Supplementary Fig. 3e, f, g), which are all suggest dominant 100 ka cycle^{9,37–39}. The loess magnetic susceptibility has been suggested to be strongly affected by the dilution effect of the dust sedimentation rate^{23,40}. Loess carbon isotopes in inorganic carbonates ($\delta^{13}\text{C}_{\text{IC}}$) have been adopted as a terrestrial vegetation proxy, and further the monsoon hydroclimate indicators in northern China, are controlled by the effects of both temperature and rainfall conditions^{9,39}. The beryllium isotope (¹⁰Be) concentration in loess can probably also be influenced by sediment grain size⁴¹ despite the dust flux, recycled ¹⁰Be and geomagnetic effects have been removed³⁷. Thus, such complex responses in proxies of loess magnetic susceptibilities, carbon and beryllium isotopes likely diminish the 23 ka cycle recorded in rainfall changes in northern China. The spectral analysis of our rainfall record also suggests stronger power at the precession band than at the eccentricity band (Fig. 2c, d), corresponding to the simulated power ratio distributions of the 23 ka to 100 ka annual rainfall cycles (Fig. 1a) and indicating the dominance of precession cyclicity in affecting the hydroclimate of northern China. Such dominant 23 ka cyclical changes in northern China rainfall have also been observed in previous rainfall records in the Yellow River mouth⁴² and Tengger Desert²⁵ (Supplementary Fig. 3h, i).

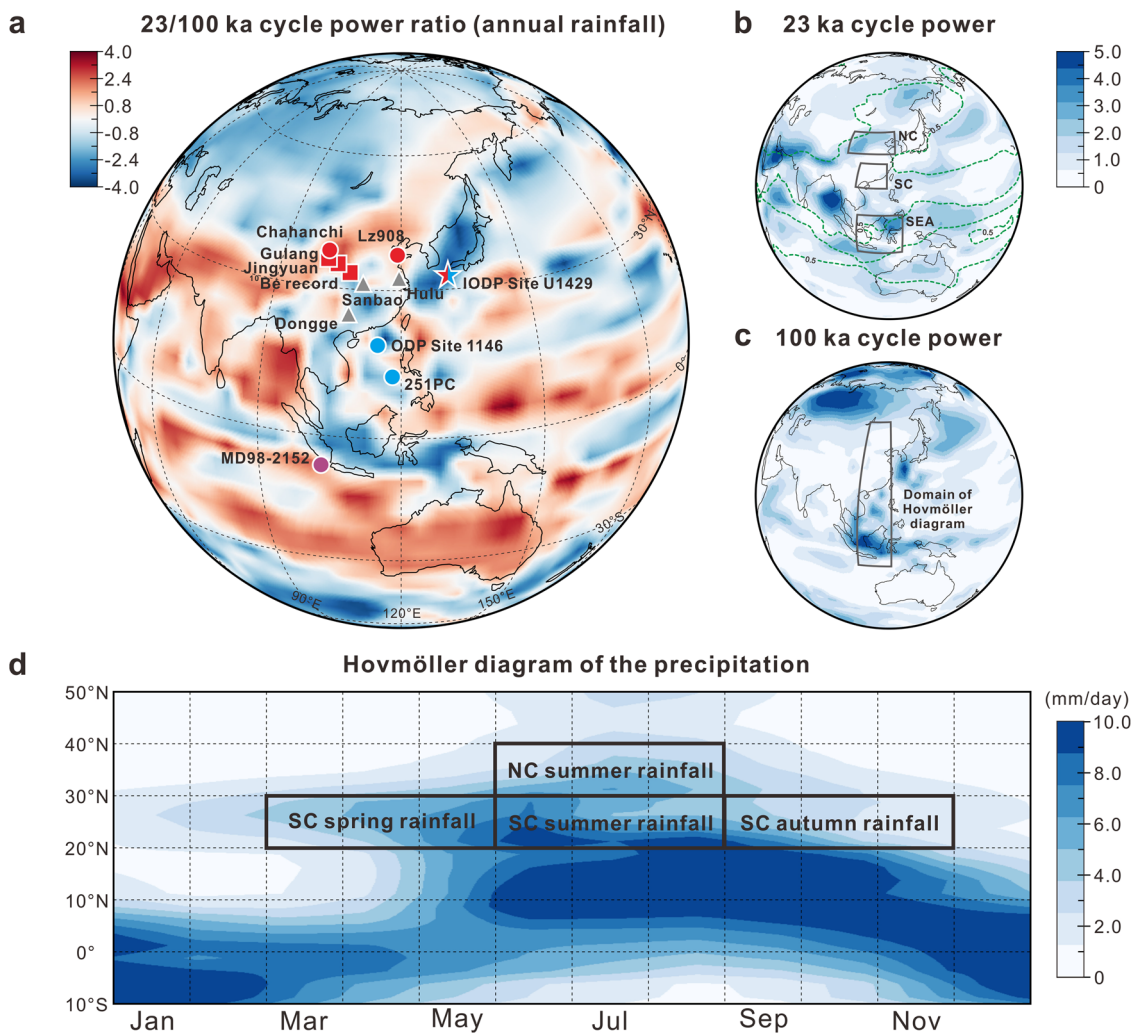


Fig. 1 Location of the study site and East-Southeast Asian hydroclimate cyclicality. **a** Simulated cyclicality of the late Quaternary hydroclimate in East-Southeast Asia. Positive values indicate that the 23 ka cycle of annual rainfall variabilities (natural log ratio, unitless) was stronger than the 100 ka cycle. The star denotes IODP Site U1429 (this study); the northern China records have been shown in red, including Chinese loess sections collected in Gulang and Jingyuan^{9,39} and ¹⁰Be record³⁷, sediment borehole of Chahanchi Lake in the Tengger Desert²⁵ and coastal sediment core Lz908,⁴² the southern China records including ODP Site 1146¹² and 251PC⁵³ have been shown in blue; the southeast Asian record of MD98-2152¹⁷ has been shown in purple. Note that the half red and half blue in symbol of IODP Site U1429 has been used to indicate both northern China rainfall based on silicate weathering proxy (this study) and southern China rainfall based on seawater $\delta^{18}\text{O}$ ¹¹ at this site. Besides, the grey triangles represent the locations of stalagmite records in northern China (NC, 33–43°N, 100–122°E), southern China (SC, 18–28°N, 105–120°E) and Southeast Asia (SEA, 10°S–8°N, 105–125°E). The green dashed line shows the simulated monsoon domains of the last 1000-year of the 300 ka simulation. The definition of monsoon domain follows⁸⁶ where annual range of rainfall >1.5 mm/day. **c** The 100 ka cycle power of annual rainfall with selected boxes exhibiting a Hovmöller diagram (10°S–50°N, 105–120°E) of the precipitation climatology across East-Southeast Asia. The powers in **b** and **c** are estimated using the power spectrum of annual rainfall time series during the last 300 ka over each model gridcell, and are averaged over the 23 ka and 100 ka period band, respectively. **d** A Hovmöller diagram of the precipitation climatology across East-Southeast Asia. The timings of the spring, summer and autumn rainfall stages in northern and southern China are also shown, suggesting the annual rainfall in northern China largely fell during the summer months, but in southern China largely occurs during the spring, summer and autumn months. In the figure, the Climate Prediction Center (CPC) Merged Analysis of Precipitation (CMAP) dataset spanning 1981 to 2010 provided by the NOAA/OAR/ESRL PSL was used.

Dominant glacial-interglacial cyclicality of rainfall variability in southern China. Explicit rainfall records cover glacial-interglacial cycle in southern China are currently lacking. Precipitation isotopes (e.g., stalagmite $\delta^{18}\text{O}$ and leaf wax $\delta^2\text{H}$) are informative hydrologic tracers that are commonly used to reconstruct hydroclimate conditions in Asian monsoon regions^{12,16,43–45}, although the complicated interpretations of these proxies depend on the rainfall amount, moisture transport and monsoon wind intensity changes^{46–49}.

The leaf wax $\delta^2\text{H}$ record at ODP Site 1146 in the northern South China Sea exhibits a dominant 100 ka cycle and relatively

light isotopic values during glacial periods (Fig. 2e)¹². Such depleted glacial $\delta^2\text{H}$ values have also been observed in a previously conducted water isotope-enabled climate simulation¹⁶. Some studies proposed that changes in the ratio of local Pacific Ocean- to remote Indian Ocean-sourced moisture that reaches eastern China could probably regulate these rainfall isotopes^{46,50}. However, during glacial periods, expansive ice sheets strengthened the pressure gradient between the East Asian continent and the Pacific Ocean, as well as enhance the Western North Pacific Subtropical High, and thus increased the amount of moisture

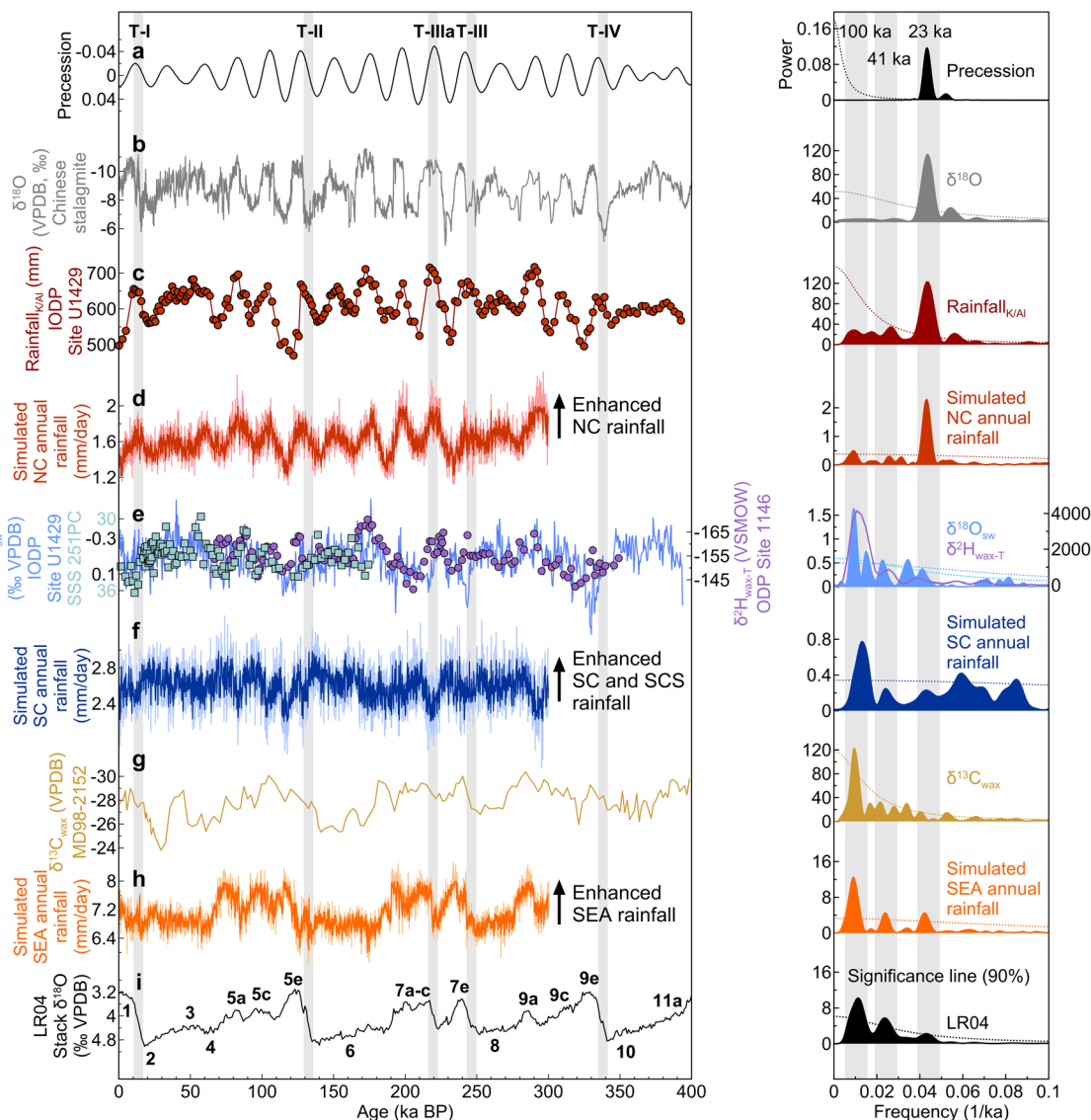


Fig. 2 Reconstructed and simulated East-Southeast Asian hydroclimate conditions and comparison with precession and benthic foraminiferal $\delta^{18}\text{O}$ records (left), as well as their corresponding spectral analysis results (right). **a** Precession⁸⁷. **b** Chinese stalagmite $\delta^{18}\text{O}$ record⁴⁴. **c** Rainfall_{K/AI} record at IODP Site U1429 indicates the rainfall in northern China (this study). **d** Simulated rainfall in northern China (this study, box NC in Fig. 1b). **e** The $\delta^{18}\text{O}_{\text{sw}}$ record obtained at IODP Site U1429¹¹, the rainfall $\delta^2\text{H}$ record at ODP Site 1146¹² (marked by circles), and the SSS record of core 251PC in the eastern South China Sea⁵³ (marked by rectangles). All of them indicate the rainfall in southern China and the South China Sea. **f** Simulated rainfall in southern China (this study, box SC in Fig. 1b). **g** $\delta^{13}\text{C}_{\text{wax}}$ record MD98-2152 from southern Sumatra¹⁷ indicate the rainfall in the western regions of Southeast Asia. **h** Simulated Southeast Asian rainfall (this study, box SEA in Fig. 1b). **i** LR04 stacked benthic $\delta^{18}\text{O}$ curve⁷². Spectral analysis has been performed with PAST software;⁸⁸ the window function is rectangle. The gray vertical bars mark the timing of glacial terminations and orbital periodicities, as shown in the left and right panels, respectively.

advected from the South China Sea and tropical Pacific Ocean to eastern China⁴⁶, leading to the enrichment of rainfall isotopes. This cannot explain the observed depleted glacial $\delta^2\text{H}$ values in this record of southern China.

A previous interpretation also linked the depleted glacial $\delta^2\text{H}$ at ODP Site 1146 to the increased rainout along the long moisture transport path over the emergent continental shelf during the glacial periods¹¹. A major challenge to this perspective is other low-latitude precipitation isotope records including Borneo stalagmite $\delta^{18}\text{O}$ records^{43,51} and southern Sumatra $\delta^2\text{H}$ record¹⁶ in the western Maritime Continent with broad shelf regions all suggest strong glacial-interglacial cycles, but characterized by the heavier isotopes during glacial periods. These contradictions indicate that the shelf exposure effect on longer moisture

transport path was probably not the main driver of depleted rainfall isotopes during glacial periods in southern China.

Hence, this leaf wax $\delta^2\text{H}$ record can be largely interpreted as a rainfall proxy in southern China, rather than the results of moisture transport and shelf exposure effect. This can be supported by the iTraCE simulation results, which suggest positive annual, June-July-August (JJA), March-April-May (MAM) and September-October-November (SON) rainfall anomalies in most regions of southern China, accompanied by negative $\delta^{18}\text{O}$ anomalies at the last glacial maximum (LGM) relative to 10 ka (Supplementary Fig. 4).

The Yangtze River Valley rainfall and runoff proxy of seawater $\delta^{18}\text{O}$ record at IODP Site U1429 is also dominated by glacial-interglacial cycles (Fig. 2e). This record has been reconstructed based on the high correlation between modern rainfall in Yangtze

River Valley and salinity at northeastern East China Sea^{11,52}. Evaporation effects on the surface salinity in northeastern East China Sea is minimal because precipitation plus runoff dominates over evaporation¹¹. This Yangtze River Valley rainfall record shows an identical trend as the leaf wax $\delta^2\text{H}$ record at ODP Site 1146 and a previously published sea surface salinity (SSS) record in the South China Sea⁵³ (Fig. 2e). The high consistency among these records is not a coincidence but most likely implies their response to local rainfall variations.

All of these records suggest dominant glacial-interglacial cycles with relatively wet conditions in southern China and the South China Sea during glacial periods. They show large consistencies with our modeled annual rainfall results in southern China, except for some differences in the fluctuation amplitudes at ~40–60 ka and ~150–180 ka and some precession scale deviations (Fig. 2f). Such discrepancies probably result from the differences between the domain of the model box, and the region that can be covered by these rainfall proxies, as well as from the age bias between modeling and rainfall reconstructions. Besides, relatively wet glacial periods in southern China have also been observed in reconstructions based on pollen databases^{54–56} and magnetic investigations⁵⁷ (Supplementary Fig. 5), as well as in LGM topsoil moisture and net precipitation simulations based on fully coupled climate models^{58,59}.

Dominant glacial-interglacial cyclicality of rainfall variability in western Maritime Continent. Critical understanding of hydroclimate indication in rainfall isotopes of Southeast Asia remains lacking. Paleoclimate studies have mainly associated changes of rainfall isotopes in this region with rainfall amount⁶⁰, moisture transport^{61,62}, moisture convergence¹⁶ and global ocean $\delta^{18}\text{O}$ variance with glaciation⁴³. In our iTraCE results, annual and JJA simulation between 20 ka and 10 ka suggest positive $\delta^{18}\text{O}$ loading corresponding to decreased rainfall in Sumatra and southern Borneo; however, most regions of Sumatra and Borneo suggest decreased spring and autumn rainfall corresponding to negative $\delta^{18}\text{O}$ (Supplementary Fig. 4). These complex seasonal patterns suggest large uncertainty in the interpretation of rainfall isotopes as rainfall amount in this region.

Here, a leaf wax $\delta^{13}\text{C}$ record from MD98-2152 in southern Sumatra offshore has been used to indicate past rainfall changes of the western Maritime Continent (Fig. 2g). Variations in this leaf wax $\delta^{13}\text{C}$ record mainly depend on the transition between C_3 and C_4 plant in Sumatra¹⁷. C_4 plants are more tolerant of high temperatures and arid climates than C_3 plants, so they are often utilized to reconstruct the local rainfall seasonality^{17,63}. Generally, this leaf wax $\delta^{13}\text{C}$ record has enriched $\delta^{13}\text{C}$ values during glacial relative to the interglacial periods, suggesting that the 100 ka cycle is the dominant frequency. Enriched $\delta^{13}\text{C}$ values during glacial periods indicate more C_4 plants and higher rainfall seasonality (enhanced dry season) in Sumatra¹⁷. This is consistent with our annual rainfall simulation results in this region (Fig. 2h), which suggests a relatively drier western Maritime Continent during glacial periods.

Forcing of northern China rainfall changes. Here we simulated the annual and seasonal rainfall differences between LGM and 10 ka with regards to the full forcing (TraCE-all) and single forcing (TraCE-ORB, TraCE-GHG and TraCE-ICE) simulations, in order to reveal rainfall changes during glacial-interglacial cycles and their forcing mechanisms. The annual, JJA, MAM and SON rainfall differences in TraCE-all all suggest a drier northern China during LGM than 10 ka (Fig. 3a, e, i). More prominent negative loading of JJA rainfall difference than that during MAM and SON indicates a dominant summer rainfall contribution in a year round in this region. This is consistent with the modern observation of seasonal cycle in northern China rainfall (Fig. 1d).

Coherent variations between the annual and summer rainfall in our 300-ka model simulation also support the leading role of summer rainfall (Supplementary Fig. 6a, b). The JJA rainfall differences over northern China of TraCE-all simulation is similar with that forced by TraCE-ORB and TraCE-GHG, indicating the combination effects of ORB and GHG forcings on local rainfall (Fig. 3e–g). However, given the dominant glacial-interglacial mode of variability in atmospheric CO_2 concentrations, the dominance of precession cycle in northern China rainfall record implies that insolation plays a leading role in local hydroclimate changes.

Our reconstructed northern China rainfall record shows highly consistent trend with Chinese cave stalagmite $\delta^{18}\text{O}$ record (Fig. 2b–d), which has been considered as an indicator of summer monsoon intensity and is driven by upstream depletion of moisture in an increasing number of works based on data-model approaches in recent years^{23,28,32,64,65}. This suggests the linear response of rainfall in northern China to East Asian summer monsoon wind intensity across the glacial-interglacial cycles. Such relationship can also be observed in the modern hydroclimate, which shows highly correlation coefficients between northern China rainfall and summer southerly wind intensity^{9,28}. With increased insolation, the surface temperatures increase more over land than over the oceans, leading to an increased land-sea temperature contrast, which enhances the southerly wind transport of moisture to northern China and thus increasing monsoon rainfall in this region⁶⁶. Our simulated rainfall and moisture flux differences between 56 ka (a high insolation stage in glacial period) and present show stronger JJA rainfall and moisture transport in northern China, providing a strong support for summer monsoon winds could still penetrate northern China and bring rainfall deep inland during high insolation stage in the glaciation (Fig. 4b).

Forcing of southern China rainfall changes. The annual, MAM and SON rainfall differences in TraCE-all suggest stronger rainfall occurred in the most regions of southern China and South China Sea during LGM than 10 ka (Fig. 3a, i). This simulated rainfall anomaly between LGM and 10 ka has also been found in a previous study⁶⁷. The JJA rainfall difference suggests a relatively dry strip extends from southwestern China to northern South China Sea; other regions of southern China and South China Sea were wetter during LGM than 10 ka (Fig. 3e). Thus the relatively stronger local rainfall during glacial periods should result from the combined effects of JJA, MAM and SON rainfall. This is consistent with the modern observation of the seasonal cycle of rainfall changes (Fig. 1d). It has been proposed that rainfall amount in southern China are evenly split between summer and non-summer months¹². A recent model simulation of hydroclimate conditions during the last deglacial period in southern China also highlighted the role of autumn rainfall³¹. This again emphasizes the importance of proxy interpretation, as summer and annual rainfall should both be carefully evaluated in this region⁶⁵. The similar rainfall responses over this region reflected in the TraCE-all, TraCE-ORB and TraCE-ICE forcings suggest that rainfall was largely driven by a combination of ICE and ORB forcings (Fig. 3a, b, d–f, h–j, l). However, the observed dominant glacial-interglacial mode of local rainfall variations indicates that it should be firstly driven by ice-sheet forcing.

During glacial periods, the expansion of high-latitude ice sheets intensified the Siberian High, resulting in anomalous northwesterly winds⁶⁸, which brought cold and dry air to southern China and the South China Sea and enhanced convergence with warm-wet air masses transported by southwesterly winds in the spring and autumn months, thus strengthening rainfall in these regions (Fig. 5c). Thus dominant glacial-interglacial cycle in

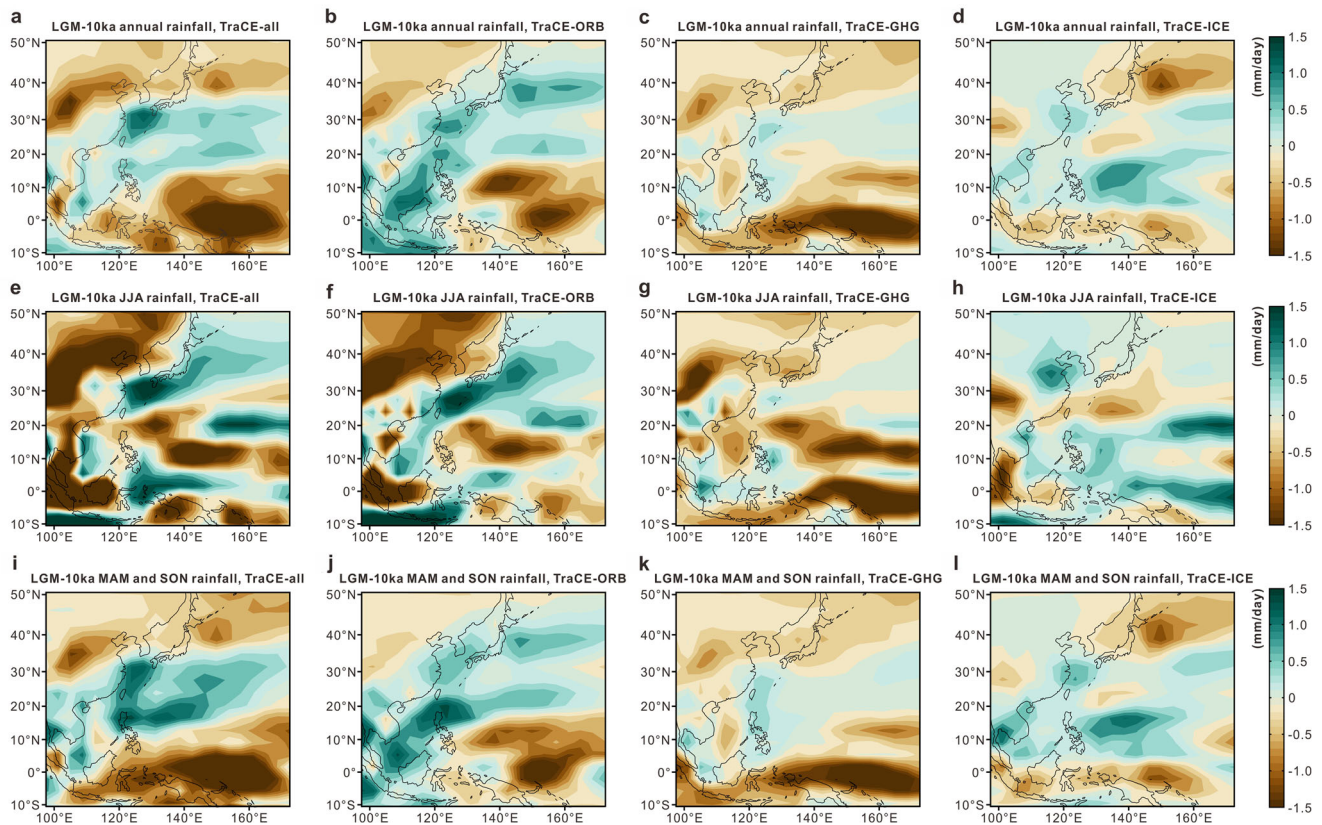


Fig. 3 Simulated seasonal rainfall differences between the LGM and 10 ka in East-Southeast Asia. a–d Annual rainfall responses to TraCE-all, TraCE-ORB, TraCE-GHG and TraCE-ICE forcings, respectively. **e–h** and **i–l** The same as **a–d** but for boreal summer (JJA), spring (MAM) and autumn (SON) rainfall, respectively.

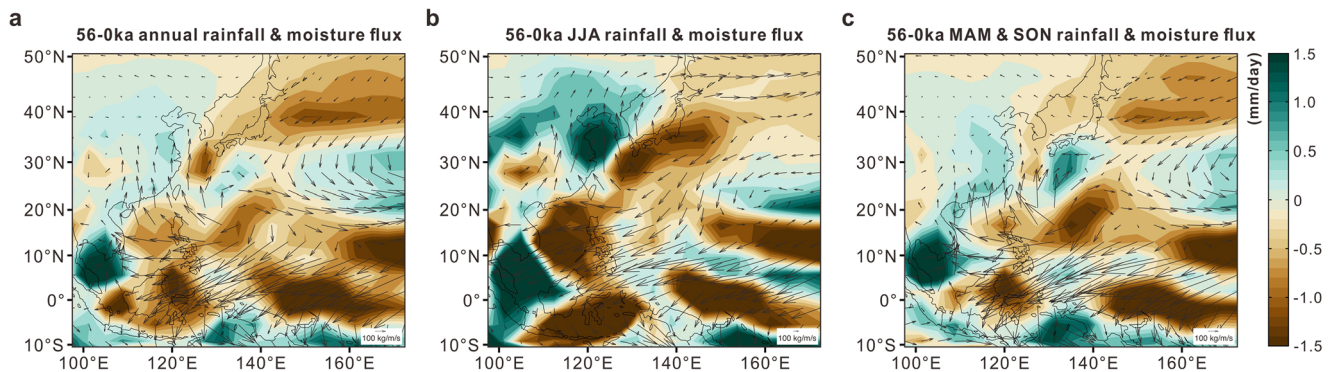


Fig. 4 Full forcing simulation of rainfall and moisture flux (arrows, kg/m/s) differences between 56 ka and present. a annual, **b** JJA, **c** MAM and SON.

annual rainfall probably largely depends on the intervention of spring and autumn rainfall. That's the reason why remarkable differences exist in cyclicity and variation trend between annual and summer rainfall over the southern China, which suggest dominant 100 ka cycle in annual rainfall but 23 ka cycle in summer rainfall, and relatively stronger annual rainfall during glacial periods (Supplementary Fig. 6c, d).

Forcing of Southeast Asian rainfall changes. The JJA, MAM and SON rainfall changes all accounted for the observed weakened glacial rainfall in Southeast Asia (Fig. 3a, e, i). Similar rainfall responses over this region reflected in the TraCE-all and single-forcing simulations suggest that rainfall changes over the western Maritime Continent were forced by a combination of GHG and ICE forcings, whereas ORB forcing was mainly present on the eastern

side (Fig. 3a, c–e, g–i, k, l). In addition, ORB forcing also played a role in JJA rainfall of the western Maritime Continent (Fig. 3f).

Previous studies proposed the exposure of Sunda Shelf cooled the surface relative to the surrounding ocean and weakened the local ascending motions and air convection, thus resulting in less rainfall occurring in this region^{17,69}. In our simulation, divergence over Sumatra and Borneo of JJA moisture supplied from eastern Indian Ocean during glacials may suppress local rainfall (Fig. 5b). Cooler sea surface temperature in eastern Indian Ocean response to the exposure of Sunda Shelf⁷⁰ probably favor such moisture transport. This nearby moisture supply may explain the positive rainfall $\delta^{18}\text{O}$ in our iTraCE results (Supplementary Fig. 4e). During spring and autumn, increased meridional SST gradient associated with high-latitude ice sheet expansion produced and maintained anticyclone in western Pacific³¹. This anticyclone promoted the anomalous

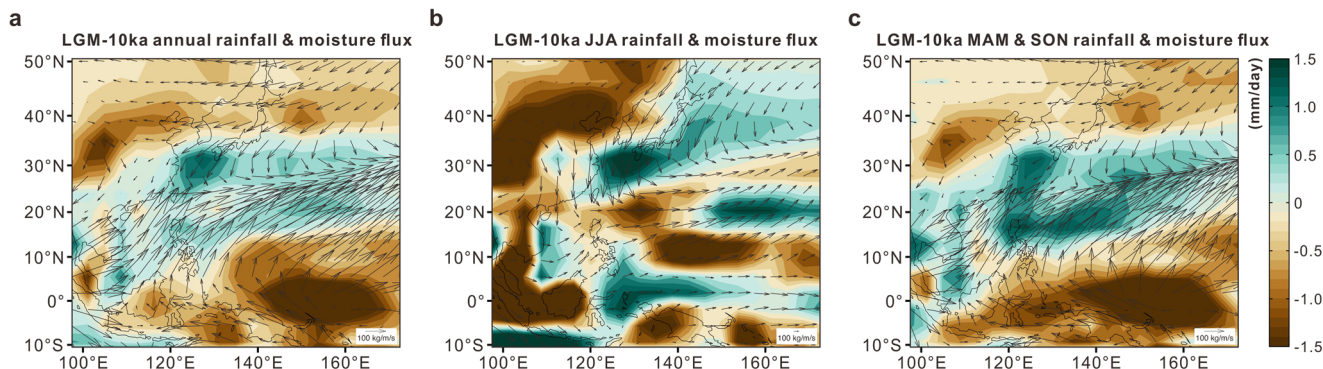


Fig. 5 Full forcing simulation of rainfall and moisture flux (arrows, kg/m/s) differences between LGM and 10 ka. **a** annual, **b** JJA, **c** MAM and SON.

moisture transport to Borneo and Sumatra, led to convergence with moisture derived from eastern Indian Ocean, thus resulted in wetter northern Sunda Shelf and parts of southern Sumatra and north-western coast of Borneo, but drier other regions of Indonesia (Fig. 5c). Besides, such remote moisture source of western Pacific can explain the negative rainfall $\delta^{18}\text{O}$ values of most regions of Indonesia observed in iTraCE simulation (Supplementary Fig. 4f).

Conclusions

This study provides a quantitative reconstruction of rainfall in northern China from marine sediments throughout the last four glacial-interglacial cycles. Combined with multiple model simulations, the ideal precession cycle of rainfall variations in northern China has been uncovered. Our results also reveal a dominant glacial-interglacial cycle in southern China-South China Sea and Southeast Asian rainfall changes, with more abundant rainfall in the former region but less rainfall in the latter during glacial periods. In contrast with previous views, we propose a reversed latitude dependence of cyclicity in the East-Southeast Asia hydroclimate, which is mainly controlled by the different responses of seasonal rainfall to insolation, ice sheet and greenhouse gas forcings.

Our study explains many of the existing controversies regarding the orbital cycles associated with rainfall variations among proxies and model simulations. Of particular importance is the highlighting of seasonal contributions to orbital-scale of rainfall changes. The large proportions of spring and autumn rainfall in southern China indicate that rainfall proxies previously established in this region cannot be simply interpreted as summer rainfall indexes. This finding can be used to reexamine the proposed heterogeneous East Asian summer monsoon rainfall variability on multiple time scales, and sheds light on the Asian hydroclimate conditions associated with high-low-latitude climate interactions in the past and future.

Materials and methods

Site location and age model. IODP Site U1429 (31°37.04'N, 128°59.85'E) is located on the western continental slope of the northeastern East China Sea in the western North Pacific at a water depth of 732 m (Supplementary Fig. 1a). At this site, three holes were cored to a composite depth below the seafloor (CCSF-D) of 200 m. The lithology of the section recovered from the study site is mainly composed of calcareous nannofossil ooze and calcareous nannofossil-rich clay, with tephra layers and minor dispersed volcanoclastic materials throughout the succession⁷¹. The age model covering the last 400 ka at Site U1429 was developed by¹¹ by correlating the $\delta^{18}\text{O}$ record obtained from benthic foraminifera with the global benthic stack⁷². In addition to the core samples, surface sediment samples were taken from the Yellow River drainage basin (from upper to lower reaches: Guide, Lanzhou, Qingtongxia, Zhaojunmu, Jundu, Huayuankou, Pingyin, Beizhen, Lijin, Kenli) in dry season of 1983⁷³ (Supplementary Fig. 1a), to exclude the effect of dam construction on chemical composition of sediments⁷⁴.

Major and trace element analysis. Geochemical analyses were performed on the clay-sized (<2 μm) siliciclastic sediments collected from IODP Site U1429 and Yellow River surface sediments. The clay-sized fractions were separated based on Stoke's settling velocity principle and recovered by centrifugation⁷⁵ after organic

matter and carbonates were removed with hydrogen peroxide (15%) and acetic acid (25%) treatments, respectively. The samples were then rinsed with deionized water three times and dried at 80 °C before being ground into powder.

The pretreated sediments were digested by a concentrated HF + HNO₃ + HClO₄ mixture in Teflon vessels for the subsequent elemental analysis. The major and trace element concentrations were determined at the Institute of Oceanology, Chinese Academy of Sciences (IOCAS), using a Thermo Icap6300 inductively coupled plasma-atomic emission spectrometer (ICP-AES) and a Perkin-Elmer ELAN DRC II ICP-mass spectrometer (ICP-MS), respectively^{76,77}. Several United States Geological Survey (USGS) and Chinese rock and sediment standards (BCR-2, BHVO-2, GBW07315 and GBW07316) and blanks were repeatedly digested and analyzed in parallel with the samples to monitor the quality of the ICP-MS and ICP-AES measurements. The results were generally within the range of $\pm 6\%$ of the certified values. The analytical precisions were generally better than 1% for major elements and 3% for trace elements.

Climate models and simulations. The fully coupled NCAR-CCSM3 model^{26,27,78,79} was employed in this work; this model contains active atmosphere, land, ocean and sea ice components. The model has a spatial resolution of $\sim 3.75^\circ$ for the atmosphere (26 vertical layers) and land, a variable latitudinal resolution ($\sim 0.9^\circ$ near the equator, becomes coarser poleward) and longitudinal resolution of $\sim 3.6^\circ$ for the ocean (25 vertical layers) and sea ice.

To investigate rainfall changes across East to Southeast Asia in the recent glacial-interglacial cycles, we analyzed transient simulation results (hereafter ORB + GHG + ICE) driven by the response to orbital, greenhouse gas and continental ice-sheet forcings over the last 300 ka. The simulation was initialized from the pre-industrial climate conditions which represents an interglacial state. Then the simulation was forced by transient boundary conditions of the orbital parameters (precession, obliquity and eccentricity), greenhouse gases (CO₂ and CH₄ concentration), and continental ice-sheets (thickness and extent). Notably, the acceleration technique was used to save computational resources. Orbital parameters and greenhouse gas concentrations were multiplied by a factor of 100; therefore, 1 model year in the simulation represents real-time climate evolution over 100 years. The continental ice sheets (mainly over Antarctica, North America and Northern Europe) were updated temporally (every 1000 or 500 years) using the ICE-5G (VM2) reconstruction product²⁷. More details of the model set-up and potential caveats can be found in²⁶.

To elucidate the forcing mechanisms on different timescales, we also analyzed the transient climate conditions over the last 21,000 years (TraCE-21 ka) using the same fully coupled NCAR-CCSM3 model. In these full TraCE simulation, the model was forced with orbital insolation (ORB), greenhouse gas (CO₂), meltwater flux (MWF), and continental ice sheet (ICE) forcings. TraCE simulations were not accelerated. We also focused on three sensitivity experiments driven by ORB (TraCE-ORB), ICE (TraCE-ICE) and GHG (TraCE-GHG) variations to better understand the forcing signals at 23 ka and 10 ka²⁹, while the millennial-timescale climate variability induced by fresh water discharge due to melting ice-sheets (reproduced in MWF) was not investigated. All TraCE simulations were conducted at the same low spatial resolution as the ORB + GHG + ICE data⁷⁹. The modeled and post processed atmospheric data used to calculate decadal mean seasonal averages were derived from the Climate Data Gateway at NCAR (<https://www.earthsystemgrid.org/>). Many model works provide an overview of the model performance of the low-resolution CCSM3 in terms of orbital-timescale monsoon evolution in East Asia and India^{11,64,80}. For instance, the model can reasonably reproduce low-level southeasterly penetrating deep into northern China⁶⁴ and the spatially heterogeneous of summer monsoon rainfall distribution between northern and southern China¹¹.

To test the relationship between the rainfall amount and water isotope ($\delta^{18}\text{O}$) record in East-Southeast Asia, iTraCE simulations based on iCESM were also conducted. This modeling process was conducted largely following the modeling strategy of TraCE-21 ka but with water isotopes enabled^{30,31,81}. The iCESM1.3 model is composed of a community atmosphere model (CAM5.3)⁸², the Parallel Ocean Program, version 2 (POP2)⁸³, the Los Alamos Sea Ice Model, version 4

(CICE4)⁸⁴, and the Community Land Model, version 4 (CLM4)⁸⁵. The resolution of the atmosphere and land data was approximately 2° (1.9° in latitude and 2.5° in longitude), with 30 vertical levels in the atmosphere; the resolution of the ocean and sea ice data was 1° horizontally (gx1v6), with 60 vertical levels in the ocean. The simulations performed herein covered the climate evolution process from 22 ka to 11 ka and considered the transient forcings associated with the ORB, ICE and GHG forcings (more details regarding these simulations can be found in ref. 32).

Data availability

All proxy and simulation data are available online for download at Zenodo (<https://doi.org/10.5281/zenodo.7431072>).

Received: 21 March 2022; Accepted: 23 December 2022;

Published online: 04 January 2023

References

- An, Z. et al. Global monsoon dynamics and climate change. *Annual Rev. Earth Planetary Sci.* **43**, 29–77 (2015).
- Imbrie, J. et al. On the structure and origin of major glaciation cycles 2. The 100,000-year cycle. *Paleoceanography* **8**, 699–735 (1993).
- Merlis, T. M., Schneider, T., Bordoni, S. & Eisenman, I. The tropical precipitation response to orbital precession. *J. Climate*. **26**, 2010–2021 (2013).
- Huang, E. et al. Dole effect as a measurement of the low-latitude hydrological cycle over the past 800 ka. *Sci. Adv.* **6**, eaba4823 (2020).
- Partridge, T., Demenocal, P., Lorentz, S., Paiker, M. & Vogel, J. Orbital forcing of climate over South Africa: a 200,000-year rainfall record from the Pretoria Saltpan. *Quaternary Sci. Rev.* **16**, 1125–1133 (1997).
- Tachikawa, K., Cartapanis, O., Vidal, L., Beaufort, L., Barlyaeva, T. & Bard, E. The precession phase of hydrological variability in the Western Pacific Warm Pool during the past 400 ka. *Quaternary Sci. Rev.* **30**, 3716–3727 (2011).
- Hou, A. et al. Insolation and greenhouse gas forcing of the South American monsoon system across three glacial-interglacial cycles. *Geophys. Res. Lett.* **47**, e2020GL087948 (2020).
- Cheng, H. et al. Eastern North American climate in phase with fall insolation throughout the last three glacial-interglacial cycles. *Earth Planetary Sci. Lett.* **522**, 125–134 (2019).
- Sun, Y. et al. Astronomical and glacial forcing of East Asian summer monsoon variability. *Quaternary Sci. Rev.* **115**, 132–142 (2015).
- Wagner, B. et al. Mediterranean winter rainfall in phase with African monsoons during the past 1.36 million years. *Nature* **573**, 256–260 (2019).
- Clemens, S. et al. Precession-band variance missing from East Asian monsoon runoff. *Nat. Commun.* **9**, 3364 (2018).
- Thomas, E. K. et al. Temperature and leaf wax $\delta^2\text{H}$ records demonstrate seasonal and regional controls on Asian monsoon proxies. *Geology* **42**, 1075–1078 (2014).
- Ding, Z. The milankovitch theory of pleistocene glacial cycles: challenges and chances. *Quaternary Sci.* **26**, 710–717 (2006).
- Lyu, A., Yin, Q., Crucifix, M. & Sun, Y. Diverse regional sensitivity of summer precipitation in East Asia to ice volume, CO_2 and astronomical forcing. *Geophys. Res. Lett.* **48**, e2020GL092005 (2021).
- Windler, G., Tierney, J. E. & Anchukaitis, K. J. Glacial-interglacial shifts dominate tropical Indo-Pacific hydroclimate during the late Pleistocene. *Geophys. Res. Lett.* **48**, e2021GL093339 (2021).
- Windler, G., Tierney, J. E., Zhu, J. & Poulsen, C. J. Unraveling glacial hydroclimate in the Indo-Pacific Warm Pool: perspectives from water isotopes. *Paleoceanography Paleoclimatology*. **35**, e2020PA003985 (2020).
- Windler, G., Tierney, J. E., DiNezio, P. N., Gibson, K. & Thunell, R. Shelf exposure influence on Indo-Pacific Warm Pool climate for the last 450,000 years. *Earth Planetary Sci. Lett.* **516**, 66–76 (2019).
- Li, X., Liu, X., Qiu, L., An, Z. & Yin, Z.-Y. Transient simulation of orbital-scale precipitation variation in monsoonal East Asia and arid central Asia during the last 150 ka. *J. Geophys. Res.: Atmospheres*. **118**, 7481–7488 (2013).
- Bosmans, J. H. C. et al. Response of the Asian summer monsoons to idealized precession and obliquity forcing in a set of GCMs. *Quaternary Sci. Rev.* **188**, 121–135 (2018).
- Shi, Z., Liu, X., Sun, Y., An, Z., Liu, Z. & Kutzbach, J. Distinct responses of East Asian summer and winter monsoons to astronomical forcing. *Clim. Past*. **7**, 1363–1370 (2011).
- Battisti, D. S., Ding, Q. & Roe, G. H. Coherent pan-Asian climatic and isotopic response to orbital forcing of tropical insolation. *J. Geophys. Res.: Atmospheres*. **119**, 11997–12020 (2014).
- Lee, J.-E., Fox-Kemper, B., Horvat, C. & Ming, Y. The response of East Asian monsoon to the precessional cycle: a new study using the geophysical fluid dynamics laboratory model. *Geophys. Res. Lett.* **46**, 11388–11396 (2019).
- Cheng, H. et al. Orbital-scale Asian summer monsoon variations: Paradox and exploration. *Sci. China Earth Sci.* **64**, 529–544 (2021).
- Weber, S. L. & Tuenter, E. The impact of varying ice sheets and greenhouse gases on the intensity and timing of boreal summer monsoons. *Quaternary Sci. Rev.* **30**, 469–479 (2011).
- Liu, C. et al. Eccentricity forcing of East Asian monsoonal systems over the past 3 million years. *Proc. Natl Acad. Sci.* **118**, e2107055118 (2021).
- Lu, Z., Liu, Z., Chen, G. & Guan, J. Prominent precession band variance in ENSO intensity over the last 300,000 years. *Geophys. Res. Lett.* **46**, 9786–9795 (2019).
- Peltier, W. R. Global glacial isostasy and the surface of the ice-age earth: the Ice-5G (VM2) model and GRACE. *Annual Rev. Earth Planetary Sci.* **20**, 111–149 (2004).
- Liu, Z., Lu, Z., Wen, X., Otto-Bliesner, B. L., Timmermann, A. & Cobb, K. M. Evolution and forcing mechanisms of El Niño over the past 21,000 years. *Nature* **515**, 550–553 (2014).
- Liu, Z. et al. Transient simulation of last deglaciation with a new mechanism for Bolling-Allerød warming. *Science* **325**, 310–314 (2009).
- Brady, E. et al. The connected isotopic water cycle in the Community Earth System Model version 1. *J. Adv. Modeling Earth Sys.* **11**, 2547–2566 (2019).
- He, C. et al. Deglacial variability of South China hydroclimate heavily contributed by autumn rainfall. *Nat. Commun.* **12**, 5875 (2021).
- He, C. et al. Hydroclimate footprint of pan-Asian monsoon water isotope during the last deglaciation. *Sci. Adv.* **7**, eabe2611 (2021).
- Wang, S. et al. Reduced sediment transport in the Yellow River due to anthropogenic changes. *Nat. Geosci.* **9**, 38–41 (2016).
- Milliman, J. D. & Farnsworth, K. L. *River discharge to the coastal ocean: a global synthesis*. Cambridge University Press (2013).
- Nesbitt, H. W. & Young, G. M. Formation and diagenesis of weathering profiles. *J. Geology*. **97**, 129–147 (1989).
- Chang, J., Wei, J., Wang, Y., Yuan, M. & Guo, J. Precipitation and runoff variations in the Yellow River Basin of China. *J. Hydroinformatics*. **19**, 138–155 (2016).
- Beck, J. W. et al. A 550,000-year record of East Asian monsoon rainfall from ^{10}Be in loess. *Science* **360**, 877 (2018).
- Sun, Y., Chen, J., Clemens, S. C., Liu, Q., Ji, J. & Tada, R. East Asian monsoon variability over the last seven glacial cycles recorded by a loess sequence from the northwestern Chinese Loess Plateau. *Geochem. Geophys. Geosys.* **7**, 97–112 (2006).
- Sun, Y. et al. Diverse manifestations of the mid-Pleistocene climate transition. *Nat. Commun.* **10**, 352 (2019).
- Kong, X. et al. Loess magnetic susceptibility flux: A new proxy of East Asian monsoon precipitation. *J. Asian Earth Sci.* **201**, 104489 (2020).
- Gu, Z. et al. Five million year ^{10}Be record in Chinese loess and red-clay: climate and weathering relationships. *Earth Planetary Sci. Lett.* **144**, 273–287 (1996).
- Yi, L. et al. Late Quaternary linkage of sedimentary records to three astronomical rhythms and the Asian monsoon, inferred from a coastal borehole in the south Bohai Sea, China. *Palaeogeography, Palaeoclimatology, Palaeoecology* **329–330**, 101–117 (2012).
- Carolin, S. A. et al. Northern Borneo stalagmite records reveal West Pacific hydroclimate across MIS 5 and 6. *Earth and Planetary Science Letters* **439**, 182–193 (2016).
- Cheng, H. et al. The Asian monsoon over the past 640,000 years and ice age terminations. *Nature* **534**, 640 (2016).
- McGrath, S. M., Clemens, S. C., Huang, Y. & Yamamoto, M. Greenhouse gas and ice volume drive Pleistocene Indian summer monsoon precipitation isotope variability. *Geophys. Res. Lett.* **48**, e2020GL092249 (2021).
- Cai, Y. et al. Variability of stalagmite-inferred Indian monsoon precipitation over the past 252,000 y. *Proc. Natl Acad. Sci.* **112**, 2954 (2015).
- Conroy, J. L., Cobb, K. M. & Noone, D. Comparison of precipitation isotope variability across the tropical Pacific in observations and SWING2 model simulations. *J. Geophys. Res.: Atmospheres*. **118**, 5867–5892 (2013).
- Liu, G. et al. On the glacial-interglacial variability of the Asian monsoon in speleothem $\delta^{18}\text{O}$ records. *Sci. Adv.* **6**, eaay8189 (2021).
- Liu, Z. et al. Chinese cave records and the East Asia summer monsoon. *Quaternary Sci. Rev.* **83**, 115–128 (2014).
- Maher, B. A. & Thompson, R. Oxygen isotopes from Chinese caves: records not of monsoon rainfall but of circulation regime. *J. Quaternary Sci.* **27**, 615–624 (2012).
- Meckler, A. N., Clarkson, M. O., Cobb, K. M., Sodemann, H. & Adkins, J. F. Interglacial hydroclimate in the tropical West Pacific through the late Pleistocene. *Science* **336**, 1301–1304 (2012).
- Kubota, Y., Tada, R. & Kimoto, K. Changes in East Asian summer monsoon precipitation during the Holocene deduced from a freshwater flux

- reconstruction of the Changjiang (Yangtze River) based on the oxygen isotope mass balance in the northern East China Sea. *Clim Past*. **11**, 265–281 (2015).
53. Zhou, Q., Yin, J., Yang, X., Chen, Q., Xie, Y. & Zhang, H. Planktic foraminiferal $\delta^{18}\text{O}$ values indicate precipitation variability in the southeastern South China Sea over the last 175 ka BP. *Quaternary Sci. Rev.* **253**, 106745 (2021).
 54. Wu, H. et al. Quantitative climatic reconstruction of the Last Glacial Maximum in China. *Sci. China Earth Sci.* **62**, 1269–1278 (2019).
 55. Xue, J., Zhong, W., Xie, L. & Unkel, I. Vegetation responses to the last glacial and early Holocene environmental changes in the northern Leizhou Peninsula, south China. *Quaternary Res.* **84**, 223–231 (2015).
 56. Xiao, J., Xiao, X., Zhang, M., Shang, Z. & Chen, Y. Late Pleistocene montane vegetation and climate history from the Dajiuhe Basin in the western Hubei Province of Central China. *Rev. Palaeobotany Palynology*. **222**, 22–32 (2015).
 57. Wei, Z. et al. Late Quaternary East Asian summer monsoon variability deduced from lacustrine mineral magnetic records of Dahu swamp, southern China. *Paleoceanography Paleoclimatology*. **35**, e2019PA003796 (2020).
 58. McGee, D. Glacial-Interglacial Precipitation Changes. *Annual Rev. Marine Sci.* **12**, 525–557 (2020).
 59. Tian, Z. & Jiang, D. Revisiting last glacial maximum climate over China and East Asian monsoon using PMIP3 simulations. *Palaeogeography, Palaeoclimatology, Palaeoecology*. **453**, 115–126 (2016).
 60. Reeves, J. M. et al. Palaeoenvironmental change in tropical Australasia over the last 30,000 years—a synthesis by the OZ-INTIMATE group. *Quaternary Sci. Rev.* **74**, 97–114 (2013).
 61. Parker, S. E., Harrison, S. P., Comas-Bru, L., Kaushal, N., LeGrande, A. N. & Werner, M. A data-model approach to interpreting speleothem oxygen isotope records from monsoon regions. *Clim Past*. **17**, 1119–1138 (2021).
 62. Wurtzel, J. B. et al. Tropical Indo-Pacific hydroclimate response to North Atlantic forcing during the last deglaciation as recorded by a speleothem from Sumatra, Indonesia. *Earth Planetary Sci. Lett.* **492**, 264–278 (2018).
 63. Dubois, N. et al. Indonesian vegetation response to changes in rainfall seasonality over the past 25,000 years. *Nat. Geosci.* **7**, 513–517 (2014).
 64. Wen, X., Liu, Z., Wang, S., Cheng, J. & Zhu, J. Correlation and anti-correlation of the East Asian summer and winter monsoons during the last 21,000 years. *Nat. Commun.* **7**, 11999 (2016).
 65. Zhang, H. et al. A data-model comparison pinpoints Holocene spatiotemporal pattern of East Asian summer monsoon. *Quaternary Sci. Rev.* **261**, 106911 (2021).
 66. Ding, Y. & Chan, J. C. L. The East Asian summer monsoon: an overview. *Meteorology Atmospheric Phys.* **89**, 117–142 (2005).
 67. Dai, G., Zhang, Z., Otterà, O. H., Langebroek, P. M., Yan, Q. & Zhang, R. A Modeling Study of the Tripole Pattern of East China Precipitation Over the Past 425 ka. *J. Geophys. Res.: Atmospheres*. **126**, e2020JD033513 (2021).
 68. Hao, Q. et al. Delayed build-up of Arctic ice sheets during 400,000-year minima in insolation variability. *Nature* **490**, 393 (2012).
 69. DiNezio, P. N. & Tierney, J. E. The effect of sea level on glacial Indo-Pacific climate. *Nat. Geosci.* **6**, 485–491 (2013).
 70. Di Nezio, P. N. et al. The climate response of the Indo-Pacific warm pool to glacial sea level. *Paleoceanography* **31**, 866–894 (2016).
 71. Tada R. et al. Asian Monsoon: Onset and evolution of millennial-scale variability of Asian monsoon and its possible relation with Himalaya and Tibetan Plateau uplift. *Integrated Ocean Drilling Program Preliminary Reports* **346**, (2014).
 72. Lisiecki, L. E. & Raymo, M. E. A Pliocene-Pleistocene stack of 57 globally distributed benthic $\delta^{18}\text{O}$ records. *Paleoceanography* **20**, PA1003 (2005).
 73. Zhang, J. et al. History of Yellow River and Yangtze River delivering sediment to the Yellow Sea since 3.5 Ma: Tectonic or climate forcing? *Quaternary Sci. Rev.* **216**, 74–88 (2019).
 74. Guo, Y., Li, C., Wang, C., Xu, J., Jin, C. & Yang, S. Sediment routing and anthropogenic impact in the Huanghe river catchment, China: an investigation using Nd isotopes of river sediments. *Water Resources Res.* **57**, e2020WR028444 (2021).
 75. Zhao D. et al. Asynchronous variation in the Quaternary East Asian winter monsoon associated with the tropical Pacific ENSO-like system. *Geophys. Res. Lett.* **46**, 6955–6963 (2019).
 76. Zhao, D. et al. Provenance, sea-level and monsoon climate controls on silicate weathering of Yellow River sediment in the northern Okinawa Trough during late last glaciation. *Palaeogeography Palaeoclimatology Palaeoecology*. **490**, 227–239 (2018).
 77. Wan, S. et al. Human impact overwhelms long-term climate control of weathering and erosion in southwest China. *Geology* **43**, 439–442 (2015).
 78. Otto-Bliesner, B. L., Brady, E. C., Clauzet, G., Tomas, R., Levis, S. & Kothavala, Z. Last glacial maximum and Holocene climate in CCSM3. *J. Climate*. **19**, 2526–2544 (2006).
 79. Yeager, S. G., Shields, C. A., Large, W. G. & Hack, J. J. The low-resolution CCSM3. *J. Climate*. **19**, 2545–2566 (2006).
 80. Jalihal, C., Srinivasan, J. & Chakraborty, A. Modulation of Indian monsoon by water vapor and cloud feedback over the past 22,000 years. *Nat. Commun.* **10**, 5701 (2019).
 81. Wong, T. E., Nusbaumer, J. & Noone, D. C. Evaluation of modeled land-atmosphere exchanges with a comprehensive water isotope fractionation scheme in version 4 of the Community Land Model. *J. Adv. Modeling Earth Systems*. **9**, 978–1001 (2017).
 82. Neale, R. B. et al. Description of the NCAR community atmosphere model (CAM 5.0). NCAR Tech. Note NCAR/TN-486+STR **1**, 1–12 (2010).
 83. Smith R., Jones P., Briegleb B., Bryan P. & Yeager S. The Parallel Ocean Program (POP) reference manual: Ocean component of the Community Climate System Model (CCSM). (2010).
 84. Hunke, E. C. Thickness sensitivities in the CICE sea ice model. *Ocean Modelling*. **34**, 137–149 (2010).
 85. Oleson, K. W. et al. *Technical Description of Version 4.0 of the Community Land Model (CLM)* (No. NCAR/TN-478+STR) (University Corporation for Atmospheric Research, 2010).
 86. Wang, B. & Ding, Q. Global monsoon: Dominant mode of annual variation in the tropics. *Dynamics of Atmospheres and Oceans* **44**, 165–183 (2008).
 87. Berger, A. & Loutre, M.-F. Insolation values for the climate of the last 10 million years. *Quaternary Sci. Rev.* **10**, 297–317 (1991).
 88. Hammer, Y., Harper, D. A. & Ryan, P. D. PAST: Paleontological statistics software package for education and data analysis. *Palaeontologia Electronica*. **4**, 1–9 (2001).

Acknowledgements

We thank the Integrated Ocean Drilling Program and the scientific party and technicians of IODP Expedition 346 for obtaining the samples. We are also grateful for the helpful suggestions for proxy reconstruction and mechanism discussion from Youbin Sun. We thank the editors Sze Ling Ho and Joe Aslin, and three anonymous reviewers for their help and constructive comments. This work was supported by the National Natural Science Foundation of China (42176063) and Strategic Priority Research Program of the Chinese Academy of Sciences, China (XDB40010100) received by D.Z. and S.W., respectively, and funding from FORMAS mobility (Grant no. 2020-02267) received by Z.L.

Author contributions

D.Z. and Z.L. designed this study. D.Z. wrote the first draft of the manuscript with input from all co-authors. D.Z. carried out the major and trace element analysis on clay-sized sediments. Z.L. analyzed the 300 ka transient climate model simulation, TraCE-21ka and iTRACE. S.W. participated in sampling and directed the study. H.C. contributed to the discussion and commented on the manuscript. X.S. and A.L. discussed the results.

Competing interests

The authors declare no competing interests.

Additional information

Supplementary information The online version contains supplementary material available at <https://doi.org/10.1038/s43247-022-00670-9>.

Correspondence and requests for materials should be addressed to Debo Zhao or Zhengyao Lu.

Peer review information *Communications Earth & Environment* thanks David McGee and the other, anonymous, reviewer(s) for their contribution to the peer review of this work. Primary Handling Editors: Sze Ling Ho, Joe Aslin, Heike Langenberg. Peer reviewer reports are available.

Reprints and permission information is available at <http://www.nature.com/reprints>

Publisher's note Springer Nature remains neutral with regard to jurisdictional claims in published maps and institutional affiliations.



Open Access This article is licensed under a Creative Commons Attribution 4.0 International License, which permits use, sharing, adaptation, distribution and reproduction in any medium or format, as long as you give appropriate credit to the original author(s) and the source, provide a link to the Creative Commons license, and indicate if changes were made. The images or other third party material in this article are included in the article's Creative Commons license, unless indicated otherwise in a credit line to the material. If material is not included in the article's Creative Commons license and your intended use is not permitted by statutory regulation or exceeds the permitted use, you will need to obtain permission directly from the copyright holder. To view a copy of this license, visit <http://creativecommons.org/licenses/by/4.0/>.

© The Author(s) 2023